IJNAOE
©SNAK, 2014

Int. J. Nav. Archit. Ocean Eng. (2014) 6:269~281
http://dx.doi.org/10.2478/IJNAOE-2013-0178
pISSN: 2092-6782, eISSN: 2092-6790

Verification of CFD analysis methods for predicting the drag force and thrust power of an underwater disk robot

Tae-Hwan Joung[1], Hyeung-Sik Choi[2], Sang-Ki Jung[2], Karl Sammut[1] and Fangpo He[1]

[1]*School of Computer Science, Engineering and Mathematics, Flinders University, Adelaide, Australia*
[2]*Division of Mechanical and Energy Systems Engineering, Korea Maritime University, Busan, Korea*

ABSTRACT: *This paper examines the suitability of using the Computational Fluid Dynamics (CFD) tools, ANSYS-CFX, as an initial analysis tool for predicting the drag and propulsion performance (thrust and torque) of a concept underwater vehicle design. In order to select an appropriate thruster that will achieve the required speed of the Underwater Disk Robot (UDR), the ANSYS-CFX tools were used to predict the drag force of the UDR. Vertical Planar Motion Mechanism (VPMM) test simulations (i.e. pure heaving and pure pitching motion) by CFD motion analysis were carried out with the CFD software. The CFD results reveal the distribution of hydrodynamic values (velocity, pressure, etc.) of the UDR for these motion studies. Finally, CFD bollard pull test simulations were performed and compared with the experimental bollard pull test results conducted in a model basin. The experimental results confirm the suitability of using the ANSYS-CFX tools for predicting the behavior of concept vehicles early on in their design process.*

KEY WORDS: Underwater disk robot (UDR); Computational fluid dynamics (CFD); Drag force; Planar motion mechanism (PMM) test simulation; Bollard pull test; Thrust; Torque.

INTRODUCTION

A large variety of underwater robots have been developed by many research institutes over the last two decades. Some of the more successful of these robots are now being employed for scientific, commercial and military purposes. Research into developing more efficient underwater robots is being conducted with a view to improving mission duration (Yuh, 2000).

A new type of the underwater robot called an UDR has been developed and its design evaluated by CFD analysis such as a resistance test, propulsion test (bollard pull test) and Planar Motion Mechanism (PMM) test simulation. The body of the UDR is designed as a disk shaped vehicle in order to minimize the effect of external disturbances such as currents and waves. The UDR is composed of hull and frame structure, three vertical thrusters, three horizontal thrusters, a control system and sensors. The thrusters are mounted axi-symmetrically at an angle of 120 degrees to enable the UDR to navigate along any direction by vector summation with the propulsion controller.

Resistance (drag) testing, Propeller Open Water (POW) testing and PMM testing are essential steps that are required to predict the drag force, propulsion power and motion performance of an underwater vehicle. Conventionally, the tests for the prediction of drag, propulsion performance and motion of an underwater vehicle are carried out in a large model basin equipped with a towing carriage, and dynamometer, making the test process expensive. The development of commercial codes for CFD

Corresponding author: *Tae-Hwan Joung*, e-mail: *cpjoung@naver.com*

analysis now make it possible to predict drag and propulsion performance of a ship or submersible vehicle such as an underwater robot without using a physical model test basin (Joung et al., 2012).

There are many efforts at predicting drag forces of underwater vehicles by CFD analysis and validating CFD simulation methods in design processes (Yu and Su, 2010, Bellingham et al., 2010). CFD simulations are also compared with in-service data for the self-propelled performance of an Autonomous Underwater Vehicle (AUV) (Phillips et al., 2008). However, carrying out experimental tests for ducted propellers of underwater vehicles, or predicting performance of an UDR, is rarely reported.

In the work reported in this article, CFD analysis was first used to conduct the resistance test necessary to predict the total drag force for selecting an appropriate thruster that will achieve the required speed of the UDR. Pure heaving motion and pure pitching motion studies were then carried out to emulate the VPMM test by CFD motion analysis. The hydrodynamic forces on the UDR body and the distributions of the hydrodynamic values (velocity, pressure etc.) around the UDR body were obtained while the UDR was performing these motions.

Finally, the custom designed ducted propulsion system that is employed in the UDR was also analysed using CFD tools. The results of the CFD analysis for the ducted thruster were compared for validation purposes with the experimental test results that were obtained using a specially designed thrust measurement system. In order to further verify the validity of the CFD modeling process, a CFD model of a commercial thruster was developed and analysed and the estimated thrust performance characteristics compared against the corresponding physical test data as supplied by the thruster manufacturer.

DRAG ESTIMATION OF THE UNDERWATER DISK ROBOT

Concept design (initial design)

The UDR, shown in Fig. 1, was designed as a streamlined disk shape to reduce the drag force on the body in the horizontal direction. The bare hull of the UDR measures 1.9*m* in diameter and 0.45*m* in height.

The design speed (NCR; Normal Continuous Rating) for the initial design of the UDR is 3.5*knots* (1.8004*m/s*) and the maximum speed (MCR; Maximum Continuous Rating) is 5*knot* (2.572*m/s*). The configuration of the thrusters is shown in Fig. 2. The three horizontal thrusters, which were custom designed, and manufactured by the Korea Maritime University, are mounted in the x, y plane at intervals of 120° to each other about the z-axis, so that the UDR can move laterally by their resultant force. The three horizontal thrusters can also rotate (±15°) about their individual mounting points using a coupled belt and pulley arrangement, to allow the vehicle to yaw. Another group of three thrusters are mounted vertically located at intervals of 120° but aligned with the z-axis to allow vertical movement of the UDR. Therefore, the UDR is designed to be able to move laterally, heave, yaw, roll and pitch by some combination of the six axi-symmetrically installed thrusters.

Fig. 1 Hull of the UDR.

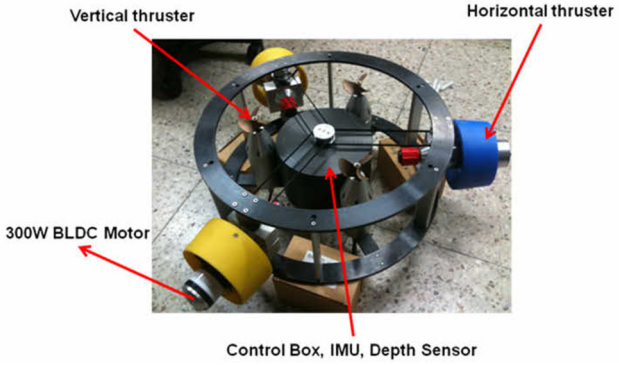

Fig. 2 Internal view of the constructed UDR.

CFD Setup for Predicting the UDR drag force

The fluid flow around the UDR has been modeled using the commercial CFD analysis code ANSYS-CFX 14.0. For these calculations, the fluid's motion is modeled using the incompressible, isothermal Reynolds-averaged-Navier-Stokes (RANS) equations in order to determine the Cartesian flow field and pressure of the water around the UDR body. The equations consist

of a general solution of the ensemble-averaged, steady-state, three dimensional Navier–Stokes equations, where the *k-ε* turbulence model (*k* is turbulence kinetic energy and *ε* is viscous dissipation rate) has been used to close the system of equations. The symmetry condition was employed to reduce computation time.

The shape of the domain is cylindrical as shown in Fig. 3 (top). The length of the domain is 8 times longer than the UDR body (8*L*) and diameter is 4 times longer (4*L*). The length of the tank was made long enough to allow the wake from the UDR body to be observed and the diameter of the tank is also long enough to reduce the wall effect.

The meshing operation was performed using ANSYS Workbench-CFX-Mesh as shown in Fig. 3 (bottom). Layered (20 layers) meshes were used for generating the boundary layer elements around the UDR body while unstructured (Tetrahedral) meshes were employed for the region far from the body as they are not suitable to resolve the boundary layers adjacent to a solid body (Nishi, 2007).

The height of cells adjacent to the walls was set to less than 20.0 y+ units for compatibility with the k-ε turbulent model at the required Reynolds numbers (ANSYS Inc., 2010; CFX-TASCow, 2002). The y+ was checked after the CFX-solve processing stage as shown in Fig. 4. The specifications for the pre-processing stage, including the mesh generation, are summarized in Table 1.

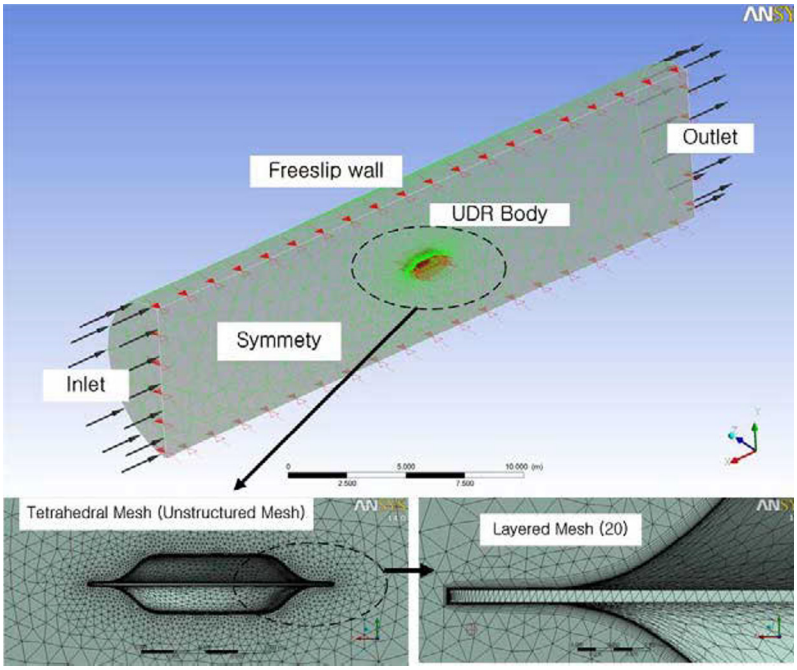

Fig. 3 Review of the pre-processing and meshing results for the CFD analysis.

Table 1 Principal conditions employed in the CFD analysis.

Water tank size	15.0*m* (Length, 8*L**) / 7.5*m* (Diameter, 4*L*)
Turbulence model	k-ε model (Scalable wall function)
Reynolds number	4.26×10^5 ~ 4.26×10^6
No. of the inflation layer	20
Y+ check	< 20.0
Total no. of elements (nodes)	413,001 (142,236)
No. of Tetrahedral elements	210,441
No. of Prism elements	202,560

* *L* is the UDR length along the x-axis (forward direction).

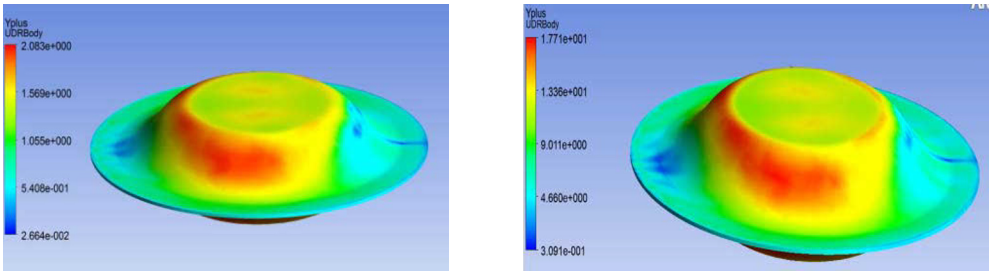

(a) 0.5*knot*. (b) @ 5*knots*.

Fig. 4 Y-plus on the UDR body.

CFD Analysis results

A mesh convergence study was performed at the design speed (3.5*knots*), and the results are displayed in Table 2. It was observed that once the number of cells for the case is reached the size of the reference, the variation in the total drag force (R_T) was small considering the significant changes made to the simulation. The reference mesh size for the case was therefore considered to be of sufficient accuracy.

The total drag force (R_T) of the UDR body, and the decomposed friction (R_F) and pressure (R_P) components, are obtained directly from the CFD analysis and shown in Table 3.

The pressure (form) drag force is obtained by calculating the integral of the pressure on the surface of the vehicle. It was found that the pressure drag force was relatively larger than the friction drag force as the speed of the UDR grows due to the pressure difference between the front and back of the body caused by its shape as shown in Fig. 5. Fig. 5 shows velocity and pressure distribution at the lowest speed (0.5 *knot*), design speed (3.5*knots*) and highest speed (5*knots*) in this simulation test.

Table 2 Result of convergence study with UDR CFD model at the design speed (@ 3.5*knots*).

Case	Number of cells	Total drag force
Reference	**413,001**	**114.46 [*N*]**
Reduced mesh size-1	612,362	113.97 [*N*]
Reduced mesh size-2	512,045	114.97 [*N*]
Increased mesh size-1	357,226	116.18 [*N*]
Increased mesh size-2	102,141	121.22 [*N*]

Table 3 Computed drag forces on the UDR.

	ANSYS-CFX			REQUIRED POWER [*W*]
Vel. [*knot*]	Friction drag (R_F) [*N*]	Pressure drag (R_P) [*N*]	Total drag (R_T) [*N*]	
0.50	0.86	1.65	2.51	0.65
1.00	3.10	6.77	9.87	5.08
1.50	6.56	15.33	21.89	16.89
2.00	11.18	27.28	38.46	39.57
2.50	16.91	42.61	59.53	76.55
3.00	23.69	61.14	84.83	130.91
3.50	**31.53**	**82.93**	**114.46**	**206.07**
4.00	40.41	107.80	148.22	304.97
4.50	50.27	135.88	186.15	430.90
5.00	60.94	167.22	228.15	586.81

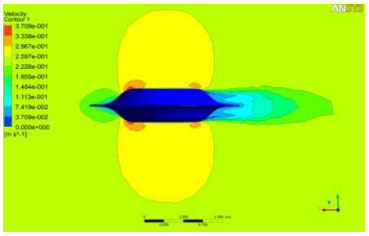

(a) @0.5*knot.*

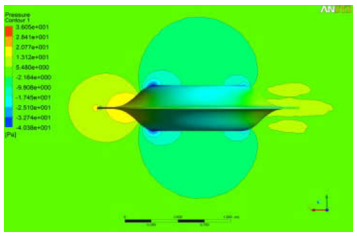

(b) @0.5*knot.*

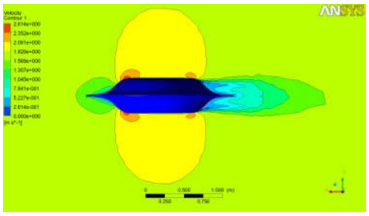

(a) @3.5*knots.*

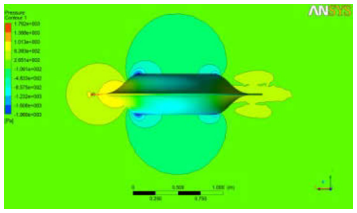

(b) @3.5*knots.*

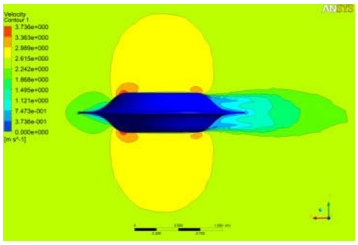

(a) @5*knots.*

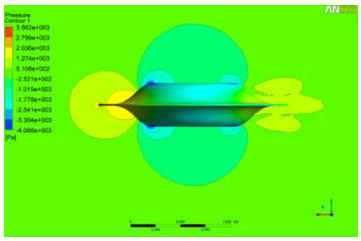

(b) @5*knots.*

Fig. 5 Velocity (a) and pressure (b) distribution at 0.5, 3.5 and 5*knots.*

SIMULATION

Definition of PMM test

A VPMM test is carried out with the aim of measuring the hydrodynamic forces on the vehicle when changing the motion of the vehicle in the vertical direction. The hydrodynamic forces from the VPMM test are obtained for the pure heaving motion and the pure pitching motion of the vehicle. The hydrodynamic forces are then used to obtain the hydrodynamic coefficients of the UDR in order to build the vehicle's control system.

For the case of pure heaving motion, the vehicle moves in a purely sinusoidal fashion with amplitude (z_0), and zero pitch angle (θ_0) as shown in Fig. 6(a). Pure pitching motion, on the other hand, is such that the vehicle moves in a sinusoidal fashion, but this time with a pitching angle (θ_0) at the centre of gravity of the vehicle body and the longitudinal body axis is oriented tangential to the path, as shown in Fig. 6(b).

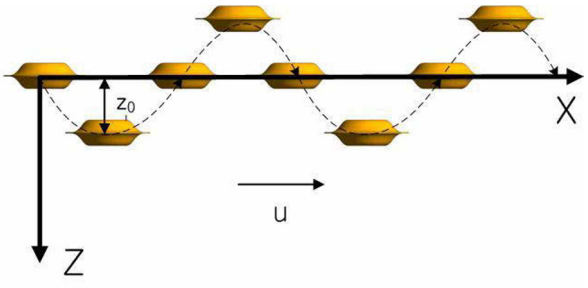

(a) Pure heaving motion.

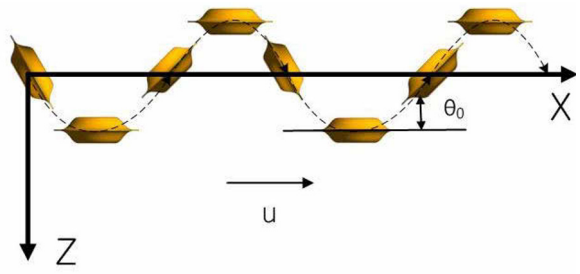

(b) Pure pitching motion.

Fig. 6 Description of pure heaving motion (a) and pure pitching motion (b).

Motion Analysis by CFD

For the purposes of this motion analysis study, the position of the body should be defined and specified in accordance with the VPMM test requirements. The motion of the UDR body is defined as shown in Fig. 7 (top) by using the ANSYS-CFX Command Language (CCL) to simulate the pure heaving and pure pitching motions.

'Tetrahedral' and 'Prism' elements were employed for generating nodes and elements in the fluid domain. A hybrid mesh is created by merging the two mesh structures, and embodied for the CFD analysis by the "ANSYS-CFX-MESH" mesh generator as shown in Fig. 7 (bottom). The mesh properties for the UDR PMM motion study are shown in Table 4.

The "Mesh-Deformation" was employed to facilitate the motion of the UDR according to time. The concerned domain moves in accordance with the UDR motion by means of the "Mesh-Deformation" ensuring that size and shape of the domain mesh does not change and affect the CFD results.

The Incompressible RANS solver has been employed for this fluid motion assuming the Reynolds number (R_n), 1.659e6. The k-ε turbulence model was used to provide solutions to the Reynolds stresses in terms of known quantities to allow closure of the RANS by ANSYS-CFX.

Table 1 Density of the model employed for the PMM Test simulations.

Total no. of Nodes	523,899
Total no. of Faces	57,180
Total no. of Elements	1,457,504
No. of *Tetrahedrals*	646,944
No. of *Prisms* (for B.C.)	810,560

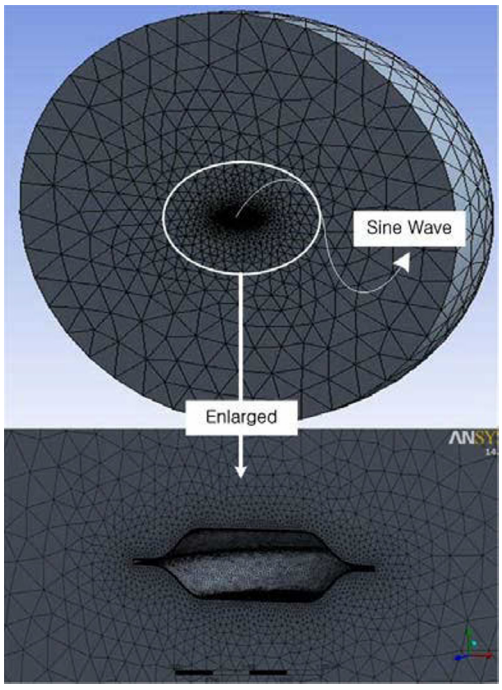

Fig. 7 Overall view of the mesh (top) and enlarged view (bottom) showing the hybrid mesh generated adjacent to the main body of the UDR.

UDR Motion analysis results by CFD

For the pure heaving motion test, the heave period (T_h) was set to 8 seconds while for the pure pitching motion test; the pitch period (T_p) was set to 12 seconds. These periods have been chosen based on the length of the UDR - 1.9*m*.

In both tests, the x-directional velocity of the vehicle was set to 1*m/s*. The total computation time (*T*) is 24 seconds and the time step (Δt) is 0.1 second for the CFD moving analysis.

Fig. 8 shows the pressure and velocity distribution around the UDR after 24 seconds from the starting point. The pressure distribution around the UDR shows that the maximum pressure occurs in the bow (667.8 Pa-Pure heaving motion; 610.7 Pa-Pure pitching motion). The pressure difference between the fore and aft of the vehicle is higher when carrying out pure heaving motion.

Although the x-directional velocity (U_0) of the vehicle is 1*m/s*, the boundary layer grows along the mid-body and the flow is accelerated as it reaches the stern. Hence, the velocity of the flow along the body is higher than the x-directional velocity of the vehicle (1.917*m/s* - Pure heaving motion; 1.186*m/s* - Pure pitching motion).

The x- and z-axis directional forces of the pure heaving motion (a) and pure pitching motion (b) obtained from the CFD analysis are shown in Fig. 9. The added mass and inertia of the vehicle are derived from these hydrodynamic forces (Lee et al., 2011).

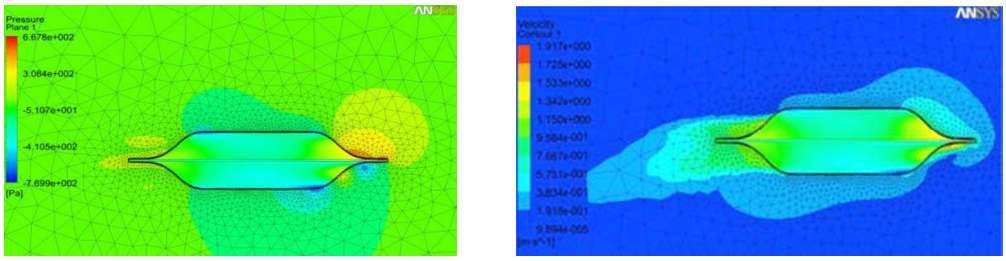

(a) Pure heaving motion (T_h=8 [*sec*] @24[*sec*]).

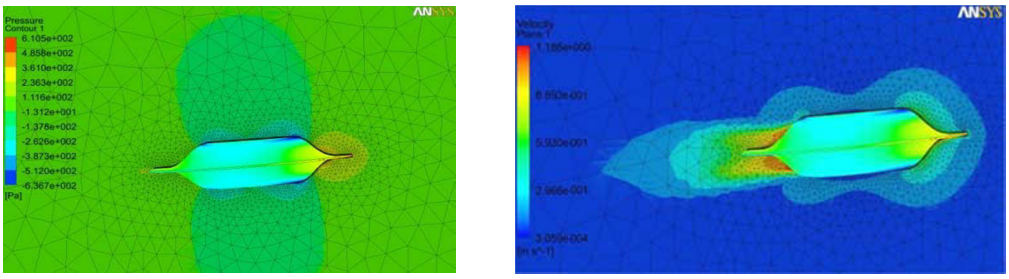

(b) Pure pitching motion (T_p=12 [*sec*] @24[*sec*]).

Fig. 8 Pressure and velocity distribution around the UDR.

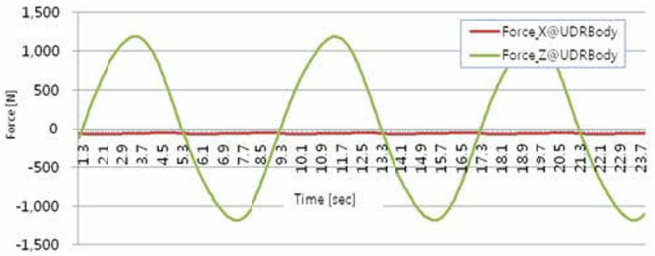

(a) Pure heaving motion (T_h=8 [*sec*]).

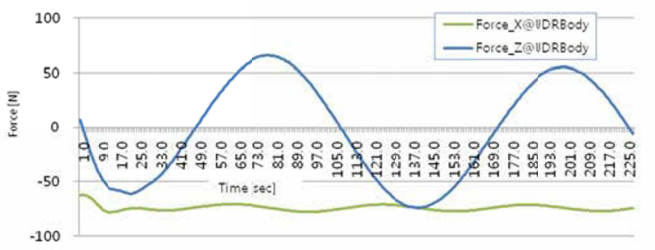

(b) Pure pitching motion (T_p=12 [*sec*]).

Fig. 9 X- and Z-directional forces on the UDR body.

CHARACTERISING THE UDR THRUSTER's THRUST POWER

The following section uses the custom-designed horizontal thrusters as a test scenario for confirming the validity of the CFD modeling approach. The discussion is limited in this paper to the horizontal thrusters. Similar modeling and analysis techniques can also be used to characterise the performance of the vertical thrusters.

The ducted propeller design is shown in Fig. 10. The propeller has seven blades, and the pitch and diameter of the blades are 12.8*mm* and 111.15*mm* (the diameter including the duct is 141.72*mm*), respectively. The diameter of the hub is 54*mm* and the gap between the inside of the duct and the blade tips is 4.5*mm*.

Bollard pull test

Bollard pull tests were carried out with nine copies of the designed 300*W* thruster. The thrusters will be installed on the UDR for horizontal thrust power.

The conventional method for measuring thrust force is not directly suitable for determining the thrust force or torque produced by a single body thruster, such as the ones used in the UDR, where the nozzle, propeller and BLDC motor are all integrated together in one module. A purpose-built thrust power test system, as shown in Fig. 11, was therefore, designed and constructed for characterizing the performance of the ducted thruster. The bollard pull thrust power of each thruster was measured with the developed thrust power measurement system. Thrust forces produced by the blades rotating in the forward direction and in the reverse direction were obtained for a range of revolution speed (*rpm*). The propeller revolution speed was controlled by electric current supplied from the controller board. The propeller revolution speed was measured with a laser tachometer and thrust powers were calculated based on the obtained voltages with the load cell. The tests were carried out with the thrust power measurement system at the Circular Water Channel (CWC) tank facility at Korea Maritime University. Fig. 12 shows the pictures taken during the bollard pull thrust test.

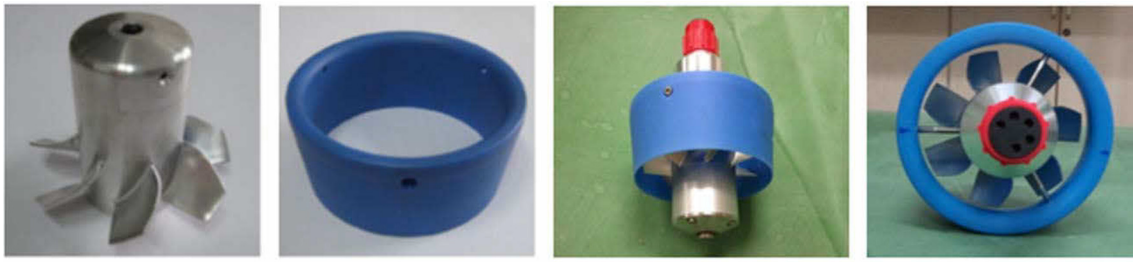

Fig. 10 The manufactured propeller, nozzle and assembled thruster.

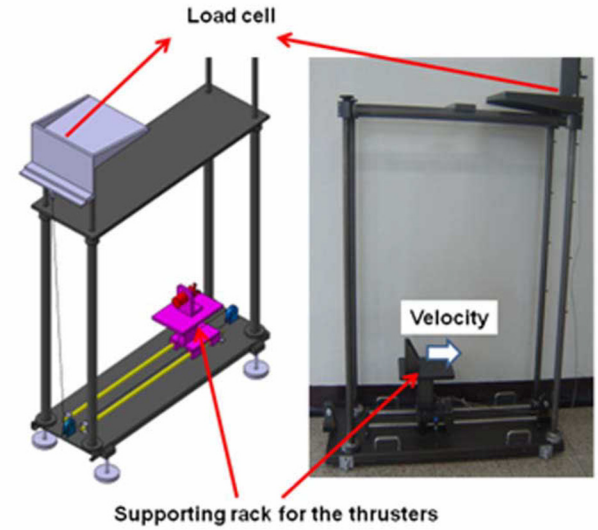

Fig. 11 Configuration of the experimental thrust measurement apparatus.

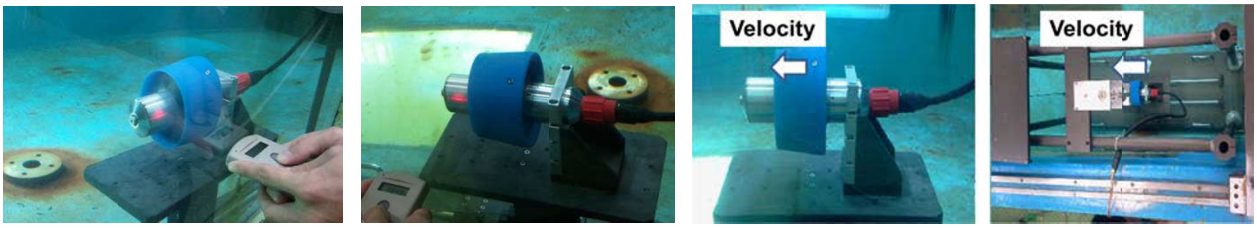

Fig. 12 Bollard pull thrust power measurement test of the 300*W* motor propulsion systems.

CFD Analysis (geometry model, mesh generation and boundary condition)

The CAD model of the ducted propeller design is shown in Fig. 13. The meshing operation, which was performed using ANSYS Workbench-CFX-Mesh, generated a mesh with 5,281,598 elements and 1,441,134 nodes. A structured layer mesh (Prism elements, 20 layers) was employed as the boundary layer. The mesh model for the CFD analysis is illustrated in Fig. 14.

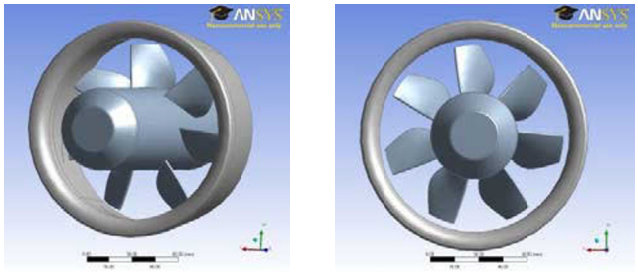

Fig. 13 The geometry of the ducted propeller.

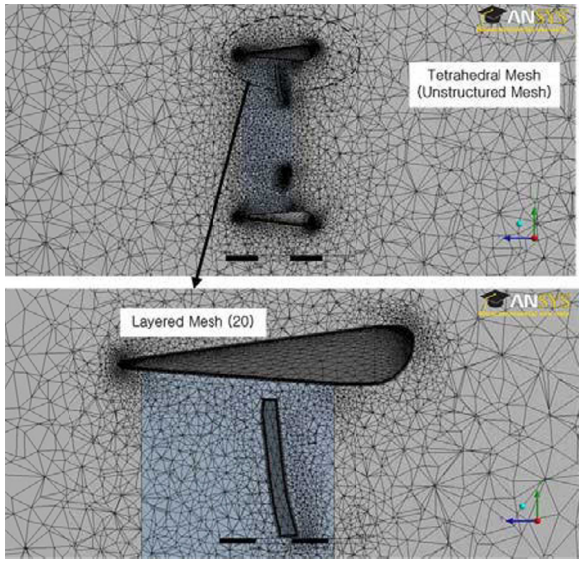

Fig. 14 Grid of the computational domain for the propulsion test (showing zoomed in section in bottom image).

The Shear Stress Transport (SST) turbulence model was used for simulating turbulence, and the modified wall function was employed to reduce the number of the elements.

Employing suitable assumptions for the simulation could help save considerable computation time in the CFD analysis. The region in the UDR thruster can, for instance, be divided into a 'rotational region' and a 'stationary region'. The Multiple Reference Frame (MRF) method can be used to conduct a simulation based on such assumptions (Wickstrom, 2007). The rotational region is defined around the blades while other regions are defined as stationary, as shown in Fig. 15. "The frozen rotor method" and the "General Grid Interface (GGI) method" were used for transferring information between the rotational region grid and the stationary region grids (ANSYS Inc., 2011).

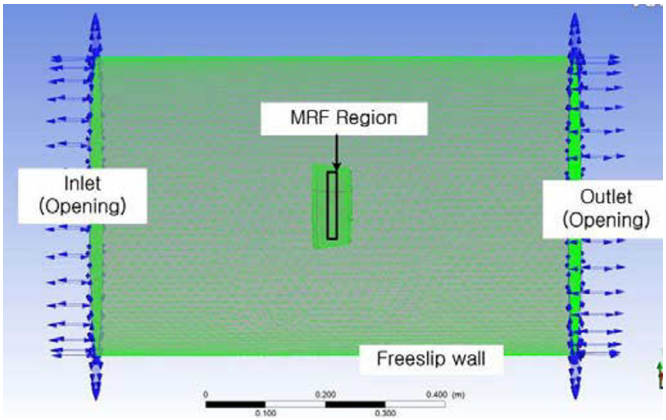

Fig. 15 Pre-processing for the propulsion test and defining the MRF region.

Results of the CFD analysis

The thrust forces and torques of the ducted propellers were obtained from CFD analysis for the range 600*rpm* to 1,300*rpm* for both forward and reverse directions.

The thrust forces and torques produced by the blades inside of the duct and the thrust forces and torques produced by the duct itself were computed separately as shown in Table 5. The thrust forces produced by the duct are about 33～39% of the thrust forces by blades when the blades are rotating in the forward direction. On the other hand, the duct thrust forces is about 45~47% of the blades' thrust forces when the blades are rotating in the reverse direction. All of the thrust forces and torques increase linearly with the rpm.

Velocity and pressure distributions on the propeller plane at the rotational speed, 600*rpm* (the lowest speed value) and 1,300*rpm* (the highest speed value), are shown front-on in Fig. 16 and side-on in Fig. 17. As shown in Fig. 16, the rotational flow forward of the blades is characterized by high velocity and low pressure. Fig. 17 reveals that the thrust force is induced by the flow and prevented losing rotational energy from the tip of each blade as water escapes from the high pressure side of the blade to the low pressure side.

A comparison of the results obtained from the CFD analysis and those obtained from the experimental tests is presented in Fig. 18. The experimental test results were obtained from the bollard pull tests with nine copies of the 300*W* thruster. The averaged value of the test results and CFD analysis result are compared. While the results for the forward direction correspond well with less than 5% errors, the differences between the results in the reverse direction are significant (up to over 100% of errors). This is because the thruster supporting structure, which is located just behind the propeller as shown in Fig. 12, affects the thrust power when it rotates in the reverse direction. The flow, therefore, is unable to enter the duct directly when rotating in the reverse direction and the reverse thrust forces are consequently low compared to those for the forward direction.

Note that the revolution speeds (*rpm*) of experimental test data are different from those of CFD analysis as the revolution speed was controlled by electric current from the controller board which was not able to adjust to the exact corresponding revolution speed.

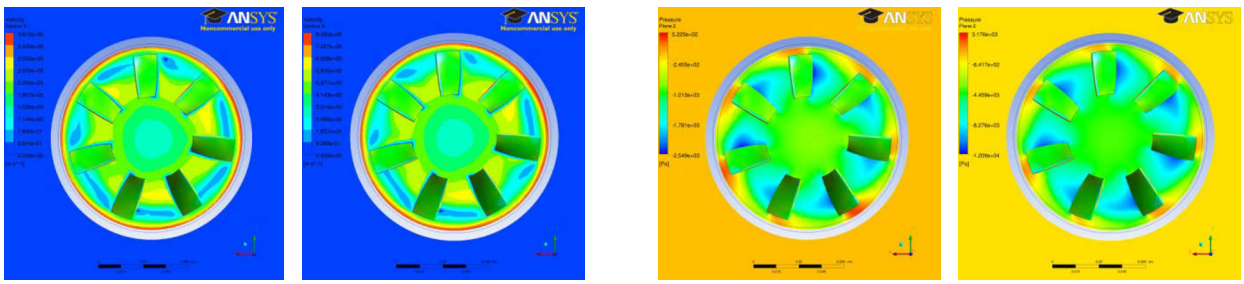

(a) Velocity distribution @ 600*rpm* (right), 1,300*rpm* (left). (b) Pressure distribution @ 600*rpm*(right), 1,300*rpm* (left).

Fig. 16 Velocity and pressure distribution in front of the propeller plane at 600*rpm* and 1,300*rpm*.

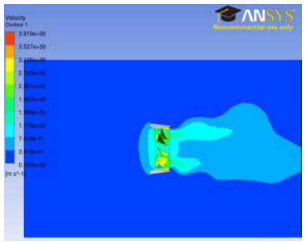

(a) Velocity distribution @ 600*rpm* (right), 1,300*rpm* (left).

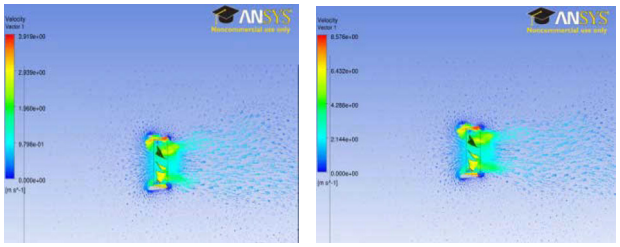

(b) Vortex distribution @ 600*rpm* (right), 1,300*rpm* (left).

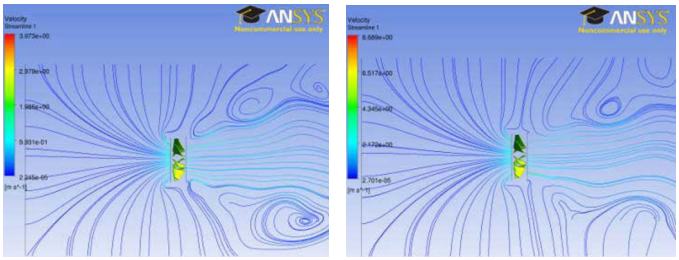

(c) Streamline distribution @ 600*rpm* (right), 1,300*rpm* (left)

Fig. 17 Velocity (a), vortex (b) and streamline (c) distribution on the mid-plane at 600*rpm* and 1,300*rpm*.

Table 5 CFD Results for forward/reverse directions of the thrusters.

CFD results for forward direction				
rpm	Thrust (All) *[N]*	Thrust (Blade) *[N]*	Thrust (Duct) *[N]*	Torque (Blades) *[N·m]*
600	6.852	4.918	1.934	-0.1980
700	9.004	6.739	2.265	-0.2660
800	11.759	8.737	3.022	-0.3483
900	15.136	10.927	4.209	-0.4351
1000	18.957	14.014	4.943	-0.5461
1100	23.054	16.878	6.176	-0.6638
1200	26.920	19.685	7.235	-0.7849
CFD results for backward direction				
rpm	Thrust (All) *[N]*	Thrust (Blade) *[N]*	Thrust (Duct) *[N]*	Torque (Blades) *[N·m]*
600	-6.718	-4.552	-2.167	0.1624
700	-9.044	-6.117	-2.927	0.2175
800	-11.864	-8.023	-3.841	0.2846
900	-15.034	-10.160	-4.874	0.3586
1,000	-18.648	-12.600	-6.048	0.4427
1,100	-22.648	-15.350	-7.298	0.5389
1,200	-26.970	-18.428	-8.542	0.6482
1,300	-31.672	-21.833	-9.839	0.7681

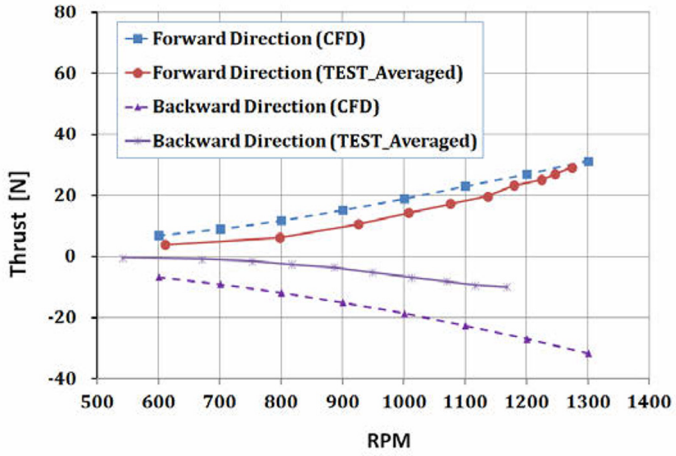

Fig. 18 Comparison of bollard pull test results for experimental test and CFD analysis.

Validation of the CFD results

The CFD modeling and analysis process was further validated by testing the approach on a commercial off the shelf motor design, the Tecnadyne Model 300 thruster (Fig. 19). The Tecnadyne thruster was modeled and meshed, and the CFD predicted thrust measurements were compared with the experimental thrust power data provided by the manufacturer (Tecnadyne Co., 2014).

The mesh is generated based on user defined parameters describing the size of the grid at surface boundaries. The simulation conditions, such as boundary condition, turbulence model are the same as those described in the previous section. The total number of grid cells was approximately 1.46 million.

The comparison is shown in Table 6. The thrust forces for the forward direction and reverse direction are all in good agreement. The errors are about 7% at the maximum rotating speed of the blades which are 1,826*rpm* and 1,890*rpm* in the forward and reverse directions, respectively. Possible reasons for the discrepancy between the predicted and measured thrust forces could include cavitation effects and increased load on the blades at the gap between the tip of the blades and inner wall of the duct, neither of which were considered when carrying out the CFD analysis. This validation confirms the reliability of the CFD method.

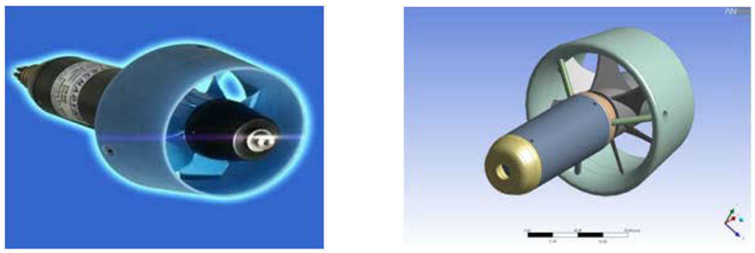

(a) Tecnadyne Model 300W thruster. (b) CAD Model for CFD anaysis

Fig. 19 Model 300 (Tecnadyne co.).

Table 2 CFD results for model 300 (Tecnadyne co.)

Type	*rpm*	Thrust (All) [*N*]	Thrust (Duct) [*N*]	Torque (Blades) *[N·m]*	Direction
CFD Results	1,826	76.65	30.349	1.1561	Forward
	1,890	28.69	6.3217	0.9648	Reverse
Technadyne Co.	1,826	71.17	-	-	Forward
	1,890	26.69	-	-	Reverse

CONCLUSIONS

Three key CFD based test procedures have been conducted on the proposed UDR design showing that the CFD analysis can be reliably used as a substitute for experimental tests in the initial design stage.

The drag estimation was conducted first using CFD analysis with a mesh convergence study performed to validate the CFD analysis. The results of the mesh convergence study indicate the mesh size selected for the CFD anlaysis was considered to be of sufficient accuracy. The CFD analysis results revealed that the CFD derived pressure (form) drag forces are relatively larger than the friction drag forces as the speed of UDR grows.

Next, the hydrodynamic forces on the UDR body were obtained from the CFD motion analysis for the pure heaving and pure pitching motion. The added mass and inertia force of the vehicle will be derived from these hydrodynamic forces in the next research step.

A test system for measuring the bollard pull thrust force of the horizontal ducted thrusters was developed and manufactured for a test, and thrust powers obtained for a sample batch of thrusters. The thrusters were then modeled and analysed, using the CFD tools, and their predicted thrust characteristics measured. The averaged value of the measured data from the bollard pull test was compared with CFD analysis data and results were shown to correspond well as the revolution speed increases for the forward case.

The CFD modeling approach was then compared with a commercial thruster of similar design (Model 300 - Tecnadyne co.) and produced close agreement in both forward and reverse cases with physical test data produced by the manufacturer.

Based on the validation studies, the CFD results have been shown to be reliable and the CFD analysis techniques employed are shown to be suitable for initial concept analysis of underwater vehicle designs.

ACKNOWLEDGEMENTS

This research was a part of the project funded by the Defense Acquisition Program Administration/Agency for defense development.

REFERENCES

ANSYS Inc., 2011. *ANSYS CFX-solver theory guide: release 14.0*. Canonsburg: ANSYS Ltd..

Bellingham, J.G., Zhang, Y., Kerwin, J.E., Erikson, J., Hobson, B., Kieft, B., Godin, M., McEwen, R., Hoover, T., Paul, J., Hamilton, A., Franklin, J. and Banka A., 2010. Efficient propulsion for the Tethys long-range autonomous underwater vehicle. *Autonomous Underwater Vehicles (AUV),* 2010 IEEE/OES, pp.1-7.

CFX-TASCow, 2002. *Computational fluid dynamics software theory documentation (Version 2.12)*. Pittsburgh: AEA Technology Engineering Software Ltd.

Joung, T.H., Sammut K., He, F. and Lee, S.K., 2012. Shape optimization of an autonomous underwater vehicle with a ducted propeller using computational fluid dynamics analysis. *International Journal of Naval Architecture & Ocean Engineering*, 4, pp.44-56.

Lee, S.K., Joung, T.H., Cheon, S.J., Jang, T.S. and Lee, J.H., 2011. Evaluation of the added mass for a spheroid-type unmanned underwater vehicle by vertical planar motion mechanism test. *International Journal of Naval Architecture and Ocean Engineering*, 3, pp.174-180.

Nishi, Y., Kashiwagi, M., Koterayama, W., Nakamura, M., Samuel S.Z.H., Yamamoto, I. and Hyakudome, T., 2007. Resistance and Propulsion Performance of an Underwater Vehicle Estimated by a CFD Method and Experiment, *ISOPE '07*, Lisbon, Spain, 1-6 July 2007, pp.2045-2052.

Phillips, A.B., Stephen, R.T. and Maaten, F., 2008. Comparisons of CFD simulations and in-service data for the self propelled performance of an autonomous underwater vehicle. *27th Symposium on Naval Hydrodynamics,* Seoul, Korea*,* 05-10 October 2008, pp.15.

Tecnadyne Co., 2014. *Model 300 DC brushless thruster*. [pdf] San Diego: Tecnadyne Co. Avilable at : < http://www.tecnadyne.com/cms/images/products/pdf/Model%20300%20Brochure.pdf> [Accessed 25 March 2014].

Wickstrom, T.B., 2007. *Fan modeling for front end cooling with CFD*. Master's thesis. Luea University of Technology of Sweden.

Yu, X. and Su, Y. 2010. Hydrodynamic performance calculation on mini-automatic underwater vehicle. *Information and Automation (ICIA), 2010 IEEE International Conference*, Harbin, 20-23 June 2010, pp.1319-1324.

Yuh, J. 2000. Design and control of autonomous underwater robots: A survey. *Autonomous Robots*, 8, pp.7-24.